Research Article

Rolling Bearing Fault Diagnosis Based on MFDFA-SPS and ELM

Yunfan Yang [1] **and Caiping Xi** [2]

^{1}Ocean College, Jiangsu University of Science and Technology, Zhenjiang 212003, China
^{2}School of Automation, Jiangsu University of Science and Technology, Zhenjiang 212003, China

Correspondence should be addressed to Caiping Xi; xicaiping@just.edu.cn

Rolling bearings, as important parts on supporting rotating shafts, frequently suffer from fatigue failures. If these rolling bearing failures are not found in time, it will have a huge impact on the whole mechanical system's operating safety and operating life. To improve the diagnosis of different faults as well as different degrees of faults, a fault diagnosis method based on the multifractal detrended fluctuation analysis (MFDFA) method-singularity power spectrum (SPS) with extreme learning machine (ELM) is proposed. First, MFDFA and SPS analyses are performed on vibration acceleration signals with different faults and different degrees of damage under the same operating conditions, the spectral parameters of stability and quantitative description of differentiation are selected for feature extraction, and then the selected six feature parameters are put into the extreme learning machine for fault classification. The effectiveness of the MFDFA-SPS feature extraction method is demonstrated by analyzing and testing the measured bearing signals. The fault diagnosis accuracy of the bearing fault signals can reach 99.2% based on the MFDFA-SPS with ELM method by using the Case Western Reserve database. The improvements are 6.79% and 18.42% compared to the fault diagnosis methods based on MFDFA with ELM and SPS with ELM. Compared with the methods based on MFDFA-SPS with LSSVM classifier and SVM classifier, the accuracy improvements are 3.54% and 4.25%, respectively. The results show that the method proposed in this paper can achieve the diagnosis of bearing faults and the method based on MFDFA-SPS with ELM is more efficient than the methods based on MFDFA-SPS with LSSVM and SVM classifiers, which is suitable for practical engineering problem-solving.

1. Introduction

Rolling bearing is one of the important components of the mechanical transmission system, due to corrosion and fatigue factors, and easy to cause bearing abrasion, pitting, and cracking failures [1]. Different faults cause different vibration noise and increased rotational resistance, making the whole transmission system life decay or even fail [2]. Therefore, it is important to ensure the normal operation of the bearings in the gearbox or drive shaft and the timely diagnosis and analysis of the structural components after a failure occurs for the normal operation of the whole unit.

Since the concept of "fractal" was first introduced by Mandelbrot in the 1980s [3], this theory of studying nonlinear systems has been widely applied in many fields and

has achieved fruitful results. The object of study of fractal theory is not smooth and irregular geometry in nature, and the bearing fault diagnosis method based on fractal theory is one of the more suitable and effective methods for bearing fault identification. Commonly used fractal theory basis includes iterative function system (IFS), fractal Brownian random field, single fractal, extended fractal, multifractal, and multifractal correlation [4, 5]. The difference in internal signal characteristics between faulty vibration signals and normal operation vibration signals is usually used in research for fault diagnosis by extracting fractal geometric change features.

For decades, scholars worldwide have proposed many methods for fault diagnosis of bearings, and the current mainstream diagnosis methods are the temperature analysis method [6] and vibration analysis method [7]. The enriched

fault features such as cyclic power spectra [8] and vibration cyclostationarity [9] parameters can be extracted when using bearing vibration signals for fault monitoring, which enables excellent diagnostic performance. The vibration analysis method mainly performs digital signal acquisition of the faulty bearing vibration signal, and its acquisition method is low cost and contains rich fault information in the vibration signal, which is convenient for real-time diagnosis and analysis.

For the analysis of nonlinear signal characteristics from the perspective of multifractals, Shao et al. [10] used the fractal box dimension method to quantitatively characterize the vibration signals of faulty bearings and found that the fractal dimensions of the faults differed from each other in their manifestations. Liu et al. [11] used detrended fluctuation analysis (DFA) to extract features of wind turbine bearing faults and proved that the fault characteristic parameters can be obtained by multifractal detrended fluctuation analysis (MFDFA). Lin and Chen [12] used the shape and location feature parameters of the multifractal spectrum obtained by the detrended fluctuation analysis and combined with the martingale repulsion to achieve the identification of the bearing damage degree. Chen et al. [13] proposed a fault prediction method based on fractal dimension using an extreme learning machine (ELM). Xiong et al. [14] used multifractal detrended fluctuation analysis methods with PSO optimized LSSVM classification method to achieve fault diagnosis of bearings. Numerous worldwide research papers have demonstrated that fractal theory can be applied to faulty bearing vibration signal processing, and the difference lies in the different effects of using different feature parameters' extraction criteria and classifiers. At present, the classifier based on combining multifractal theory and deep learning is the current niche use diagnosis method, and the diagnosis effect is fast and has a good diagnosis rate with further development trends. ELM and deep learning are complementary, and some applications combine the two to get promising results, such as using CNNs for feature extraction [15] and ELMs for classifiers.

In summary, to further realize the applicability of fractal theory to bearing fault analysis and diagnosis, this paper proposes a rolling bearing composite fault method based on MFDFA-singularity power spectrum (SPS) and ELM. The method is a quantitative description of nonlinear signals using multifractals for feature extraction. ELM is applied for further exploration of multiple classifications, and the validity of the method is verified by the actual measurement of many different types of faulty bearing signals.

This paper is organized as follows: Section 2 describes the specific model of the MFDFA algorithm; Section 3 describes the specific steps of the SPS algorithm; Section 4 presents a brief description of the ELM tool and the way to extract features using the algorithms in Sections 2 and 3; Section 5 describes the source of data, the specific feature parameter distribution, and the results of the experiments; the main findings and conclusions of the article are summarized in Section 6.

2. The Multifractal Detrended Fluctuation Analysis

The MFDFA algorithm implementation steps are described as follows [12]:

Step 1: for a times series $x(t)$ of length N, $t = 1, 2, \ldots, N$, construct a new sequence $y(t)$:

$$y(t) = \sum_{i=1}^{t} \left\{ x(i) - \frac{1}{N} \sum_{j=1}^{N} x(j) \right\}, \quad t = 1, 2, \ldots, N. \tag{1}$$

Step 2: partition the sequence $y(t)$ into $N_S = [N/S]$ mutually disjoint equal-length subintervals. There are s data points in each interval, $\max\{m + 2, 10\} \le s \le N/10$. Since the sequence length N is not necessarily an integer multiple of s, then $y(t)$ will have segments remaining, and to make the sequence of the last small segment processed, the partitioning process can be repeated from the tail of the sequence $y(t)$, thus obtaining $2N_s$ equal-length subintervals. m represents the order of polynomial fit, generally taken as $m = 1, 2, 3, \ldots$. Here, MFDFA can be denoted as MFDFA-m, and when m takes the value of 1, the method is denoted as MFDFA-1.

The mth-order polynomial $y_v^{(m)}(t)$ in the vth subinterval ($v = 1, 2, \ldots, 2N_s$) is fitted by the least-squares method, and the residual corresponding to the label t in this interval is calculated as follows:

$$\widetilde{y}_v(t) = y(t) - y_v^{(m)}(t), t = (v - 1)s + i, \quad i = 1, 2, \ldots, s. \tag{2}$$

Step 3: calculate the mean square error separately:

$$F_v(s) = \left[\frac{1}{s} \sum_{i=1}^{s} \widetilde{y}_v^2[(v - 1)s + i] \right]^{1/2}, \quad v = 1, 2, 3, \ldots, N_s,$$

$$F_v(s) = \left[\frac{1}{s} \sum_{i=1}^{s} \widetilde{y}_v^2[N - (v - N_s)s + i] \right]^{1/2}, \quad v = N_s + 1, \ldots, 2N_s. \tag{3}$$

Step 4: calculate the global root mean square value of order q, when $q \ne 0$, with

$$F_q(s) = \left\{ \frac{1}{2N_s} \sum_{v=1}^{2N_q} [F_v(s)]^q \right\}^{1/q}. \tag{4}$$

When $q = 0$, the calculation formula is

$$\ln\left[F_{q=0}(s)\right] = \frac{1}{2N_s} \sum_{v=1}^{2N_q} \ln[F_v(s)]. \tag{5}$$

Step 5: change the value of scale s to obtain the corresponding $F_q(s)$; if the signal sequence has a power-law relationship scale-invariant signal, then

$$F_q(s) \sim s^{H(q)}, \tag{6}$$

where $H(q)$ is the q-order Hurst exponent.

Find the scaling range with a linear relationship between $\log_{10}[F_q(s)]$ and $\log_{10}(s)$. Find the slope of its linear regression line, denoted as $H(q)$, by calculating the first-order polynomial fit coefficient between the scale s and the logarithmic value of the function $F_q(s)$ in the scaling range. If the relationship between $\log_{10}[F_q(s)]$ and $\log_{10}(s)$ is S-shaped curve, the value of $H(q)$ cannot be estimated.

Step 6: the correlation between $H(q)$ and the multifractal mass exponent $\tau(q)$ can be expressed as

$$\tau(q) = qH(q) - D_f, \tag{7}$$

where D_f denotes the topological dimension of the multifractal signal, and for a one-dimensional time series of signals, $D_f = 1$.

Step 7: the singularity intensity function $\alpha(q)$ and the singularity dimension $f(\alpha)$ can be obtained by the Legendre transformation:

$$\alpha(q) = \frac{d\tau(q)}{dq},$$
$$f(\alpha) = \inf_q[q\alpha(q) - \tau(9)]. \tag{8}$$

In the process of changing q value from negative to positive, if $H(q)$ remains almost constant, the relationship between q-order mass exponent $\tau(q)$ and q is linear; then, the signal has single fractal characteristics and the width of the singularity spectrum is small and tends to 0. On the contrary, if $H(q)$ changes to a large extent, the relationship between q-order mass exponent $\tau(q)$ and q is not linear; then, the signal has multifractal characteristics and the width of the singularity spectrum is large. In this paper, we use MFDFA-1 method with one-direction partition process, just do the partitioning process from head to tail of the sequence $y(t)$, thus obtaining N_s equal-length subintervals.

3. The Multifractal Singularity Power Spectrum Algorithm (SPS)

3.1. SPS Algorithm. Suppose a set of signals or time series is a continuous signal.

Defining $x_\alpha(t) = \{x(t): \alpha(x(t)) = \alpha\}$ as a fractal subband signal or a fractal subset of signal $x(t)$, the time-indexed set corresponding to $x_\alpha(t)$ constitutes the set $t(\alpha) = \{t, \alpha(x(t)) = \alpha\}$; then, $x_\alpha(t)$ is denoted as

$$x_\alpha(t) = \begin{cases} x(t), & t \in t(\alpha), \\ 0, & t \in \dfrac{[0,T]}{t(\alpha)}, \end{cases} \tag{9}$$

where $\alpha(x(t))$ is the singularity exponent of $x(t)$ at the time t. According to the theory of multifractals, $x(t)$ is a thick subset supported by a tight set $\cup_\alpha x_\alpha(t)$. Meanwhile, $x_{\alpha 1}(t), x_{\alpha 2}(t), x_{\alpha 3}(t), \ldots$ form the segments of $x(t)$, where $x_{\alpha i}(t)$ are mutually disjoint, and we obtain $x_{\alpha i}(t) \cap x_{\alpha j}(t) = \varphi, i \neq j$.

All measurable subsets constitute the set system $I = \{x_{\alpha 1}(t), x_{\alpha 2}(t), x_{\alpha 3}(t), \ldots\}$, and I is a topological measurable set. There exists a measurable function $f: I \longrightarrow \mathfrak{R}^+$, and (X, I, f) constitutes a measurable space.

Based on the singularity decomposition, we can obtain the singular subset $x_T^\alpha(t)$ of $x_T(t)$ under the fractal truncation signal. The fractal energy measure of $x_T^\alpha(t)$ can be expressed as

$$P_x^T = \int_\alpha P_x^T(\alpha) d\alpha, \tag{10}$$

where $P_x^T(\alpha)$ is the singularity measure of each fractal subset $x_T^\alpha(t)$ and the singularity power spectral density of $x_T(\alpha)$. It reflects the distribution of the fractal power of $x_T(t)$ with the singularity exponent. The fractal power analysis of the singularity fractal subset $x_T^\alpha(t)$ gives the singularity power spectrum of $x_T(t)$ as

$$p_x^T(\alpha) = \frac{1}{T(x_T(t))} \int_{-T/2}^{+} \frac{|x_T^\alpha(t)|^2}{\sqrt{1+tg^2\theta_t}} dH(x_T^\alpha(t)). \tag{11}$$

The fractal power measurement of the signal sequence $x_T(t)$ and the singularity power spectrum distribution satisfy the following relationship:

$$p_x^T = \int_\alpha p_x^T(\alpha) d\alpha$$
$$= \int_\alpha \int_{-T/2}^{+T/2} \frac{1}{T(x_T(t))} \frac{|x_T^\alpha(t)|^2}{\sqrt{1+tg^2\theta_t}} dH(x_T^\alpha(t)) d\alpha. \tag{12}$$

Therefore, the SPS distribution function of the signal $x(t)$ can be defined as a limit form:

$$P_x(\alpha) = \lim_{T \to \infty} p_x^T$$
$$= \int_{-\infty}^{+\infty} \lim_{T \to \infty} \frac{|x_T^\alpha(t)|^2}{T(x_T(t))\sqrt{1+tg^2\ \theta t}} H(x_T^\alpha(dt)), \tag{13}$$

where θ_i is the local orientation angle of the truncated signal $x_T(t)$ (equivalent to the tangent direction of a conventional curve) and $dH(x_T^\alpha(t))$ denotes the differential of the Hausdorff measure of $x_T(t)$. Based on the modulus squared of the signal, the local azimuth of the fractal time element, and the Hausdorff measure, equation (15) represents the

power distribution of the fractal signal concerning the singularity exponent. Thus, the fractal energy measurement and the singularity power spectrum satisfy the relationship

$$P_x = \int_\alpha P_x(\alpha) \mathrm{d}\alpha. \qquad (14)$$

For fractal signals with a period T or finite time support $x(t), t \in [-T/2, T/2]$. Singularity energy spectral density and singularity power spectral density functions can be defined as

$$\begin{cases} E_x(\alpha) = \int_{-T/2}^{T/2} \frac{|x_\alpha(t)|^2}{\sqrt{1 + tg^2\theta_t^\alpha}} H(x(\mathrm{d}t)), \\ \\ P_x(\alpha) = \frac{1}{T(x(t))} \int_{-T/2}^{T/2} \frac{|x_\alpha(t)|^2}{\sqrt{1 + tg^2\theta_t^\alpha}} H(x(\mathrm{d}t)). \end{cases} \qquad (15)$$

It can be obtained that the singularity power spectrum reflects the fractal energy per unit singularity exponent interval, and it reflects how the fractal energy is distributed with the variation of the singularity exponent.

3.2. Specific Steps of the SPS Algorithm. The multifractal singularity power spectrum (SPS) algorithm is a quantitative analysis method to study the correlation of a sequence [16]. The steps of the SPS algorithm are as follows:

Step 1: calculate the instantaneous singularity exponent: for a given time series $x(t)$, estimate the instantaneous singularity exponent $\alpha_x(k_n)$ of the series.

Step 2: construct the singularity subset signal: according to the instantaneous singularity exponent $\alpha_x(k_n)$, set the singularity variable change interval $[\alpha_{\min}, \alpha_{\max}]$, where $\alpha_{\min} \le \alpha_x(k_n) \le \alpha_{\max}$, and divide the interval into N_α discrete singularity exponent sets $\{\alpha_q\}, q = 1, 2, \ldots, N_\alpha + 1$ according to the singularity exponent interval equivalence, where $\alpha_1 = \alpha_{\min}$ and $\alpha_{N_\alpha + 1} = \alpha_{\max}$. N_α is the number of discretized singularity indices.

Step 3: according to the interval segment of the singularity exponent after discretization, the singularity decomposition of this time series is performed; the data points whose singularity indices fall in the interval $(\alpha_i, \alpha_{i+1}], i = 1, 2, \ldots, N_\alpha - 1$, are specified as subsets belonging to the same singularity exponent α_i, and the data points whose singularity indices fall in the interval $[\alpha_i, \alpha_{i+1}], i = N_\alpha$, are specified as subsets belonging to the same singularity exponent α_i; thus, it is possible to obtain the fractal subsets with the same singularity exponents. We denote the subset of the same singularity exponent α_q by $x(\alpha_q) = \{x(i), \alpha_x(i) = \alpha_q\}$ and the total sequence by $x = \{x(i)\} = \cup_{q=1}^{N_\alpha} \{x(\alpha_q)\}, \quad q = 1, 2, \ldots, N_\alpha$, where $x(\alpha_q)$ denotes the set of all moments in the time series and $\{x(i)\}$ has the instantaneous singularity exponent
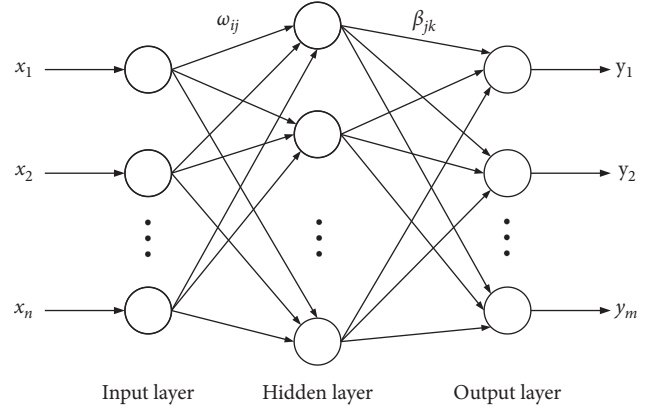

Figure 1: Structure of basic ELM.

value α_q. The number of points in the subset $x(\alpha_q)$ is related to the specific calculation, and the subset corresponding to each singularity exponent α_q is denoted as $x_{\alpha_q}(t)$.

Step 4: calculate the average power $P_x(\alpha_q)$ of the singularity subset with the same singularity exponent $\alpha = \alpha_q$: based on doing the singularity subset decomposition on $x(t)$, for the singularity subset $x_\alpha(t)$, for a given singularity exponent $\alpha = \alpha_q$, calculate the power $P_x(\alpha_q)$ of the subset (time series) with the same singularity exponent; for the convenience of presentation, denote this time series with its corresponding singularity subset $\{x(\alpha_q)\}$ as $x_{\alpha_q}(t)$ and its discrete form as $\{x_{\alpha_q}(k)\}, k = 1, 2, \ldots, N_{\alpha_q}$, where N_{α_q} is, respectively, the number of discrete point sets contained in the time series $x(t)$, as the average power $P(\alpha_q) = 1/N_{\alpha_q} \sum_k \|x_{\alpha_q}(k)\|^2$.

Step 5: calculate the singular power spectrum: iterate over all the singularity indices to obtain the singularity power spectrum $P_x(\alpha)$.

4. Extreme Learning Machine

The ELM algorithm [17] has the advantages of strong generalization ability and fast learning speed, which overcomes the disadvantages of a traditional neural network learning algorithm (such as BP neural network algorithm) that requires continuous iteration, many training times, low learning efficiency, and slow convergence speed, and is a new type of single implicit layer feedforward neural network. The ELM consists of three parts: input layer, hidden layer, and output layer, and the specific structure is shown in Figure 1.

ω_{ij} is the value of the connection between the input layer and the hidden layer, which is denoted as

$$\omega_{ij} = \begin{bmatrix} \omega_{11} & \omega_{12} & \cdots & \omega_{1n} \\ \omega_{21} & \omega_{22} & \cdots & \omega_{2n} \\ \vdots & \vdots & & \vdots \\ \omega_{l1} & \omega_{l2} & \cdots & \omega_{ln} \end{bmatrix}. \qquad (16)$$

β_{jk} is the value of the connection between the hidden layer and the output layer, which is denoted as

$$\beta_{jk} = \begin{bmatrix} \beta_{11} & \beta_{12} & \cdots & \beta_{1m} \\ \beta_{21} & \beta_{22} & \cdots & \beta_{2m} \\ \vdots & \vdots & & \vdots \\ \beta_{l1} & \beta_{l2} & \cdots & \beta_{lm} \end{bmatrix}, \tag{17}$$

where n is the number of neurons in the input layer, l is the number of neurons in the hidden layer, and m is the number of neurons in the output layer.

The threshold of the implicit layer neuron b is expressed as

$$b = \begin{bmatrix} b_1 & b_2 & \cdots & b_l \end{bmatrix}^{\mathrm{T}}. \tag{18}$$

Let $g(x)$ be the hidden layer neuron excitation function, and the output T can be expressed as the following equation:

$$T = \begin{bmatrix} t_1 & t_2 & \cdots & t_m \end{bmatrix}^{T}, \tag{19}$$

$$t_j = \begin{bmatrix} t_{1j} \\ t_{2j} \\ \vdots \\ t_{mj} \end{bmatrix} = \begin{bmatrix} \sum\limits_{i=1}^{l} \beta_{i1}(\omega_i x_j + b_i) \\ \sum\limits_{i=1}^{l} \beta_{i2}(\omega_i x_j + b_i) \\ \vdots \\ \sum\limits_{i=1}^{l} \beta_{im}(\omega_i x_j + b_i) \end{bmatrix}, \tag{20}$$

$$\omega_i = \begin{bmatrix} \omega_{i1} & \omega_{i2} & \cdots & \omega_{in} \end{bmatrix}, x_j = \begin{bmatrix} x_{1j} & x_{2j} & \cdots & x_{nj} \end{bmatrix}^{T}. \tag{21}$$

Equation (22) can also be expressed as $H\beta = T'$, where T' is the transpose matrix of T and H is the hidden output array, and the expression is

$$H = \begin{bmatrix} g(\omega_1 x_1 + b_1) & g(\omega_2 x_1 + b_2) & \cdots g(\omega_l x_1 + b_l) \\ g(\omega_1 x_2 + b_1) & g(\omega_2 x_2 + b_2) & \cdots g(\omega_l x_2 + b_l) \\ \vdots & \vdots & \vdots \\ g(\omega_1 x_Q + b_1) & g(\omega_2 x_Q + b_2) & \cdots g(\omega_l x_Q + b_l) \end{bmatrix}. \tag{22}$$

The system of equations' least squares β is

$$\min_{\beta} \| H\beta - T' \|. \tag{23}$$

The solution is $\beta' = H^{\dagger} T'$, where $H^{\dagger}$ is the Moore–Penrose generalized inverse of the output matrix of the hidden layer.

4.1. Extraction of Fractal Characteristic Features in Bearing Signals.
Statistical physics can be used to obtain a partition function for the set of probabilities of regular and irregular fractals, which uses the $q - $th power of the probability as a weight to distinguish subsets with different sizes of probabilities. In some cases, the collocation function has scale invariance of the form $\varepsilon^{\tau(q)}$ over a certain range (and over an infinite range in the case of regular fractals). Figure 2 shows
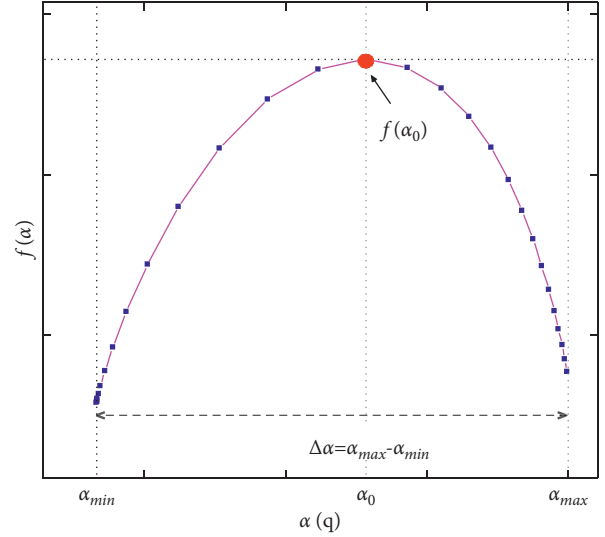

Figure 2: Multifractal spectrum.

the sketch of the multifractal spectrum used to extract features, Figure 3 shows the sketch of the Hurst exponents, and Figure 4 shows the sketch of the singularity power spectrum.

The generalized fractal dimension D_f can be obtained from $\tau(q)$, and the multifractal spectrum $f(\alpha)$ is obtained by the Legendre transform. $\alpha_{\max}$ and $f(\alpha_{\max})$ of the multifractal spectrum reflect the properties of the smallest subset of probabilities. $\alpha_{\min}$ and $f(\alpha_{\min})$ reflect the properties of the largest subset of probabilities. $f(\alpha_0)$ reflects the properties of the most contingent subset. The width $\Delta\alpha = \alpha_{\max} - \alpha_{\min}$ of the multifractal spectrum reflects the size of the probability distribution range.

The more inhomogeneous the probability distribution is, the wider the corresponding $f(\alpha)$ curve is and therefore the larger the $\Delta\alpha$ value becomes. In the practical problem of bearing fault signals such as having irregular distribution in space, the quantitative characterization of the inhomogeneous distribution of physical quantities can be achieved with the specific parameters of the multiple fractal spectrum, so it is suitable for the feature extraction of different kinds of bearing faults and different degrees of damage to achieve the diagnosis and identification of faults.

The value of the weighting factor q is also worth discussing when calculating the multifractal spectrum of the measured signal. When calculating the multifractal spectrum according to the multifractal detrended fluctuation analysis, different values of q are used to divide the signal into regions with different levels for the study. Theoretically, the larger the range of q is $(-\infty < q < \infty)$, the more complete the representation of the multifractal spectrum, but in practice, as $|q|$ increases, the computational effort increases exponentially, and the increase of q to a certain level will inevitably cause computer overflow errors. However, if the range of q is too small, the change of $f(\alpha)$ is still large for every increasement of $\Delta|q| = 1$. The obtained is only a part of the multifractal spectrum, which cannot fully reflect the probability distribution of the object of study. In general,
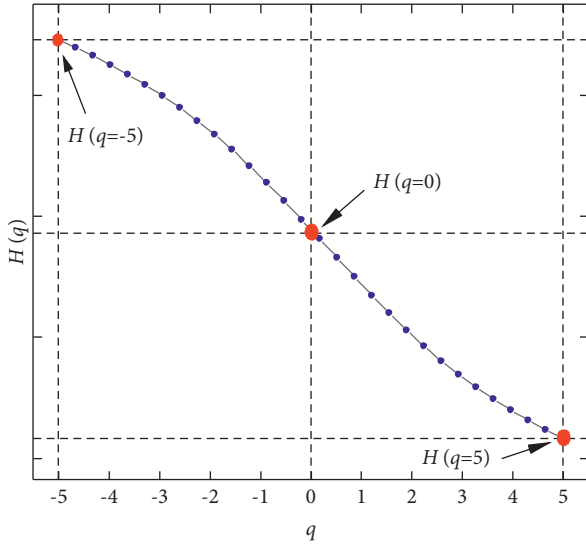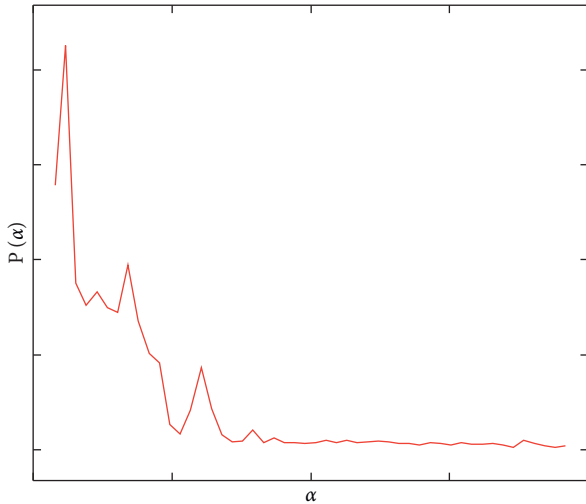
Figure 3: Hurst exponents.

Figure 4: Singularity power spectrum.

when q increases to a certain degree, regardless of the degree of a signal probability distribution, $\alpha(q)$ and $f(\alpha)$ basically do not change with the increase of q, and the range of q can be cut off. In the calculation of the stochastic fractal, a criterion for determining $|q|_{max}$ can be chosen based on this property, and a coefficient η for the variation of f with the value of q can be defined as follows:

$$\eta = \frac{f_q - f_{q-1}}{f_q - f_{max}}. \tag{24}$$

When q is infinite, $f_q = f_{q-1}$, $\eta = 0$. In the actual calculation, a value slightly larger than 0 is chosen as a criterion, for example, $\eta < 0.1\%$.

In the fractal analysis of the actual faulty bearing signal, the data are divided into segments of equal length, and each segment contains 2048 points. The efficiency can be ensured when $|q|_{max} = 5$, and without losing the multiple fractal spectrum features, the spectral parameters are characterized comprehensively.

Mandelbrot in his book "Fractals: Form, Chance, and Dimension" [15] gives a portrayal of the Hurst phenomenon, that is, river flow in which a larger-than-average flood may follow a larger flood and then, suddenly, a below-average flood, followed by more below-average floods; the whole process like there is a cycle, but not for the periodicity, and the standard statistical analysis also reveals significant correlations between observations. To separate the fractal time series from other time series, the Hurst exponent was therefore constructed to estimate the fractal dimension of the time series and the degree of series persistence or inverse persistence. When calculating the Hurst indices for measured bearing failure signals, the Hurst indices for different failures and signals with different fault levels also reflect different distributions, and the Hurst indices corresponding to different q values are taken for feature extraction when the value of $|q|_{max}$ is given. The features taken in this paper are included in Table 1.

5. Applications

5.1. Dataset Introduction. The bearing signals used in the experiments were obtained from the Bearing Data Center at the Electrical Laboratory of Case Western Reserve University, USA [18, 19]. The experimental platform consists of a 1.5 kW (2 hp) electric motor (electric motor in the left side of Figure 5), a torque sensor/translator (torque transducer and encoder in the middle of Figure 5), and a power test meter (the dynamometer in Figure 5). The rotational speed is 1772 r/min, the sampling frequency is 12 kHz, and the sampling time is 10 s. Single point faults were introduced to the test bearings using electrodischarge machining with fault diameters of 7 mils, 14 mils, 21 mils, 28 mils, and 40 mils (1 mil = 0.001 inches). SKF bearings were used for the 7, 14, and 21 mils diameter faults, and NTN equivalent bearings were used for the 28 mils and 40 mils faults. All experimental data use drive-end acceleration data, which are called vibration acceleration signals. The validity of the proposed method in this paper is verified by selecting the data of the normal state shown in Figure 6(a) and 6 fault states. The fault state data are inner-race 7 mils (slight inner-race fault) shown in Figure 6(b), inner-race 28 mils (serious inner-race fault) shown in Figure 6(c), outer-race 7 mils (slight outer-race fault) shown in Figure 6(d), outer-race 28 mils (serious outer-race fault) shown in Figure 6(e), rolling elements 7 mils (slight ball fault) shown in Figure 6(f), and rolling elements 28 mils fault (serious ball fault) shown in Figure 6(g). Because of the inconsistent length of the bearing signals, each of the data shown in Figure 6 is only for a sampling time of 5 seconds. Each type of data is divided into 50 equal segments with 2048 points per segment. We have 7 kinds of signals in different states. The validation acceleration data of each state are divided into 50 sets, and we can get 350 sets. During the analysis of the MFDFA-1 algorithm for all the selected bearing signals, the subinterval segments are taken as 12 values equally spaced and rounded between 10 and 128, and the values of q are taken as 31 values equally spaced between $[-5, 5]$ according to the rule of equation (24). The data storage format, the feature extraction

TABLE 1: The six characteristic parameters extracted by MFDFA and SPS.

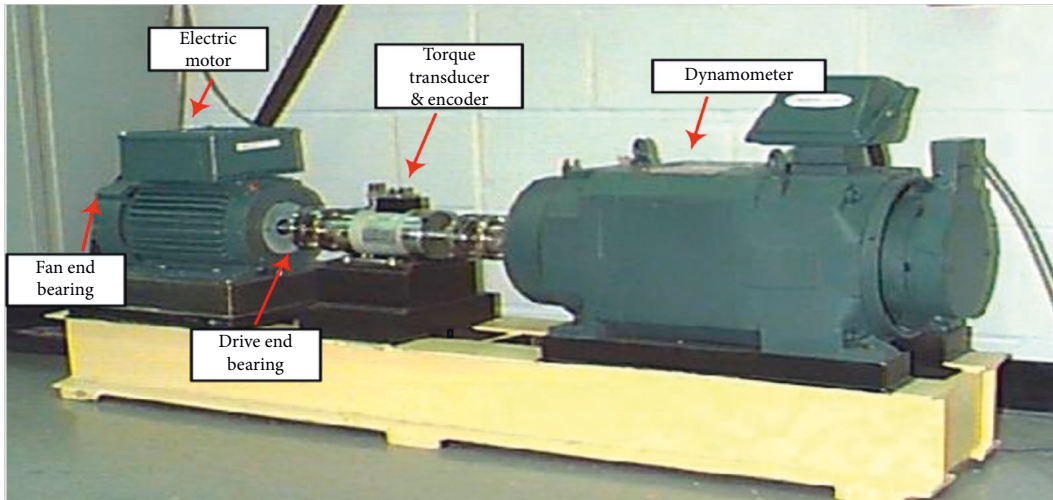|		
MFDFA	α_0	The abscissa of the multifractal spectrum vertices
	$\Delta\alpha$	The width of the multifractal spectrum
	$H(q = -5)$	The value of the hurst exponent when $q = -5$
	$H(q = 0)$	The value of the hurst exponent when $q = 0$
	$H(q = 5)$	The value of the hurst exponent when $q = 5$
SPS	$\sum P(\alpha)$	Summation of the singularity power spectrum

FIGURE 5: Experimental setup.

algorithms utilized, and the classifier application process all run on the MATLAB2020a platform. In the singularity power spectrum algorithm analysis process, the selection of subintervals is to distinguish the singularity exponent α into 50 equally spaced segments. The time-domain waveform of the vibration signal of each state bearing is shown in Figure 6.

5.2. Steps of Bearing Fault Diagnosis. To ensure the reliability of the experimental results, the bearing signals in the database are tested with the same type of bearings and the same operating conditions except for the degree of damage. The flowchart of the proposed algorithm is shown in Figure 7.

Step 1: the MFDFA and SPS algorithms are used to process the normal bearing signals and the bearing fault signals with different damage faults and different damage degrees to obtain the corresponding multiple fractal spectrum and SPS spectrum

Step 2: feature extraction using the six specific features mentioned in the above section

Step 3: the ELM classifier is used to classify the bearings in seven states, and multiple classification tools are taken to compare the classification effects

5.3. Experimental Results. First, the MFDFA and SPS algorithms were used to analyze the bearing signals in seven states, with ten samples for each state, and the corresponding multifractal spectrum and SPS spectrum were obtained, as shown in Figures 8–10.

Figure 8 shows multifractal spectra of seven signals based on MFDFA-1, where MFDFA-1 means the order of the polynomial of MFDFA is 1. It can be seen that the multifractal spectral lines in different states are hump-shaped and the spectrum widths and the location of the spectrum vertices of the corresponding multifractal spectra are different from each other. The location of the top of the multifractal spectrum of the normal bearing signal is in the rightmost part of Figure 8, and the length of the spectrum width is the shortest. The locations of the top of the spectra of the rest of faulty bearing signals are shifted to the left side of the spectrum of the normal signal. The spectrum widths of the rest of the faulty bearing signals are wider than the one of the normal signals, which indicates that the internal probability density of the faulty bearing signal has changed to different degrees.

The multifractal spectrum width of the normal bearing vibration acceleration signal is narrower than that of the faulty bearing signal, which indicates that the distribution of the probability of the amplitude of the normal operation signal is more even. An increase in the multifractal spectrum width usually implies an increase in the irregular properties within the signal. The purple solid line corresponds to a larger value of $f(\alpha_{max})$ for slight outer-race fault signal, indicating that the signal has a larger number of subsets with small probability, and the α_{min} value is the smallest, which corresponds to the subsets with maximum probability.
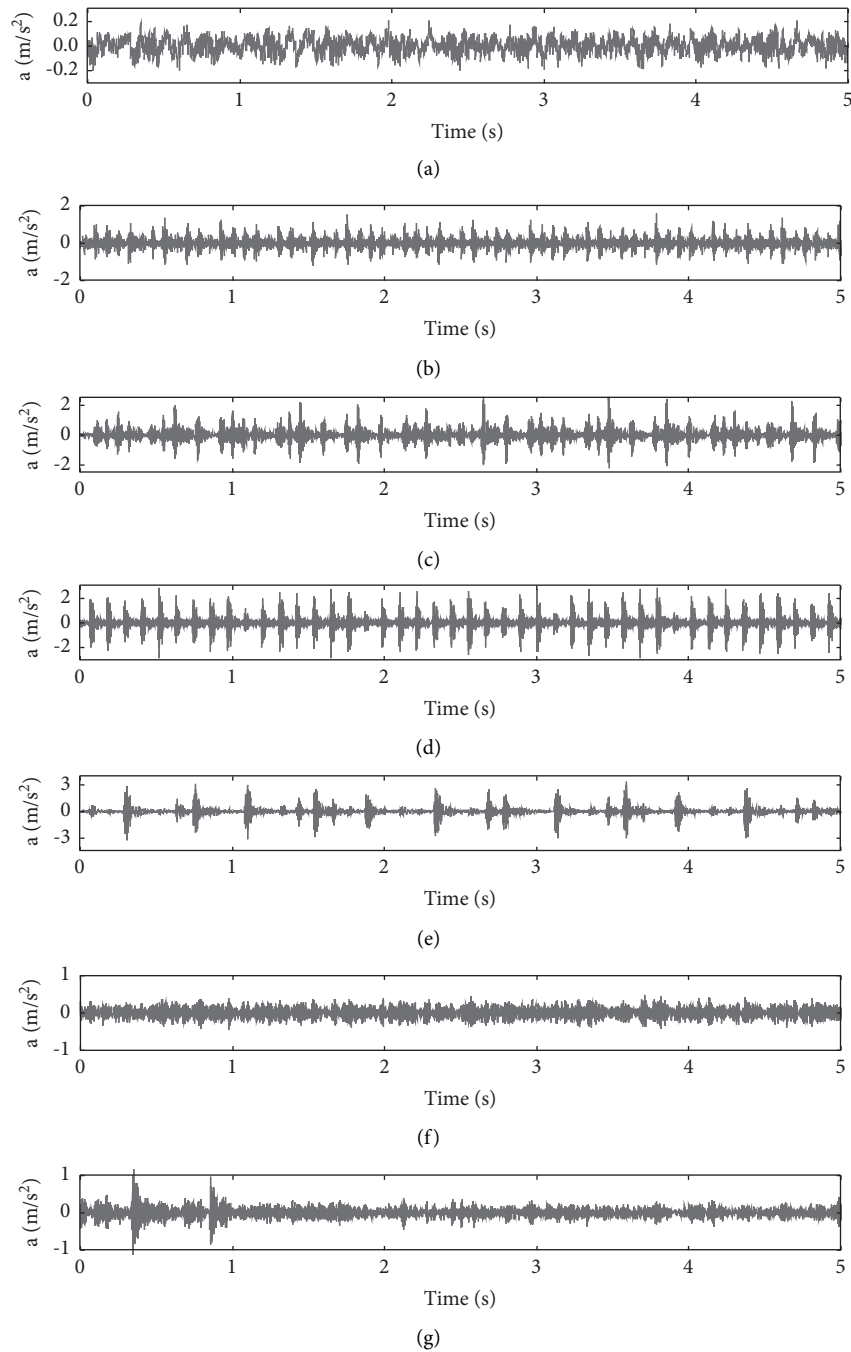
Figure 6: The waveforms of seven vibration acceleration signals in each state. (a) Normal. (b) 7 mils, slight inner-race fault. (c) 28 mils, serious inner-race fault. (d) 7 mils, slight outer-race fault. (e) 28 mils, serious outer-race fault. (f) 7 mils, slight ball fault. (g) 28 mils fault, serious ball fault.

Compared with the serious outer-race fault (olive green dotted line), the two multifractal spectra are in the shape of right hook, which indicates that the signal of the outer-race fault signal is predominated by the subset with small probability. The α_0 positions of the two signals are different, indicating that the most probable subsets are different. The spectrum widths of the two signals are similar to each other, which means that the probability density distributions of the corresponding signals are similar to each other, and the difference lies in the range of probability distributions of the two kinds of signals.

The values of $f(\alpha_{\min})$ corresponding to slight ball fault (blue-green dotted line) and serious ball fault (red solid line) are at a large level. The spectrum widths $\Delta\alpha$ of the spectra of the two kinds of signals are smaller than those of the other faults, indicating that the probability distribution of the ball

Vibration signals of rolling bearings in each status

MFDFA-1

SPS

Calculate the cumulative-sum

$$y(t) = \sum_{i=1}^{i} \left\{ x(i) - \frac{1}{N} \sum_{j=1}^{N} x(j) \right\}, t=1, 2, \ldots, N$$

Calculate the instantaneous singularity exponent $\alpha_x(k_n)$, and get $\alpha_{min} \leq \alpha_x(k_n) \leq \alpha_{max}$

Calculate the $y_v^{(1)}(t)$, $y_v^{(t)}$

Divide the singularity exponents $\alpha_x(k_n)$ into N_α equal intervals to get $N_{\alpha+1}$ singularity exponents $\{\alpha_q\}, q=1, 2, 3, \ldots, N_\alpha$

Calculate local detrended fluctuation $F_v(s)$

Calculate the subset $x_{\alpha i}(t)$ of each singularity exponent $\alpha_i, \alpha_i \in [\alpha_i, \alpha_{i+1})$, $i=1, 2, \ldots, N_\alpha-1, \alpha_i \in [\alpha_i, \alpha_{i+1}], i=N_\alpha$

Calculate Overall detrended fluctuation $F_q(s)$

Calculate the average singularity power of $P_x(\alpha_q)$ each subset of $P_x(\alpha_q) \alpha_q, q=1, 2, \ldots, N_\alpha$

Calculate the $H(q), \tau(q), \alpha(q)$, and $f(\alpha)$

Calculate the singularity power spectrum $P_x(\alpha_q)$ over all the singularity exponents $\alpha_q, q=1, 2, \ldots, N_\alpha$

Composed into a vector $[\alpha_0, \Delta_\alpha, H(q=-5), H(q=0), H(q=5), \Sigma P(\alpha)]$

Classification based on ELM

Figure 7: Flowchart of algorithm procedures.

fault signal is more uniform than the probability distributions of the other faults. The two spectrum lines are in the shape of left hook, which means that the large probability subsets dominate the signal.

The spectrum lines of slight inner-race fault (red solid line) and serious inner-race fault (blue solid line) are both left hook-shaped, and the α_0 positions of two curves are also close to each other. The values of $f(\alpha_{max})$ and $f(\alpha_{min})$ of serious inner-race fault signal are smaller than those of slight inner-race fault signal. This means that the number of both the small and large probability subsets of the serious inner-race fault signal is smaller. The value of $\Delta\alpha$ for serious inner-race fault signal is larger than that of slight inner-race fault signal, so the probability density distribution of serious
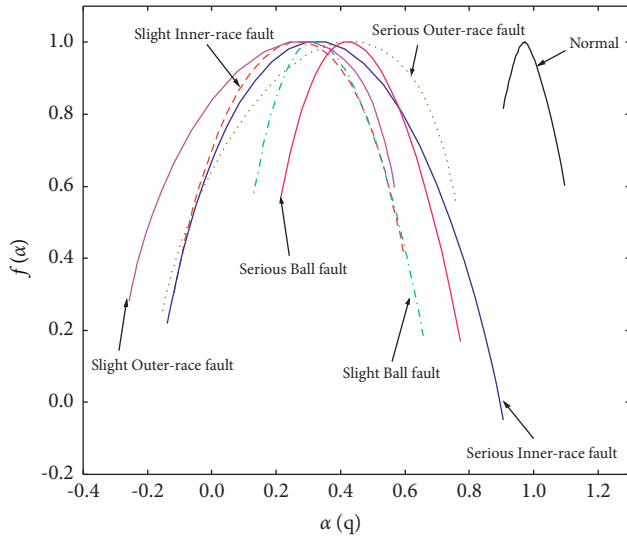
FIGURE 8: The multifractal spectra of seven signals based on MFDFA-1.

FIGURE 9: The Hurst exponents of seven signals based on MFDFA-1.

inner-race fault signal is more uneven than that of slight inner-race fault signal.

By comparing the multifractal spectra of signals with the same fault and different degrees of damage, it can be found that the multifractal spectra of signals with different degrees of damage for the same fault have similar shapes (left hook or right hook), but the difference lies in the difference in the uniformity of the probability density distribution (the size of $\Delta\alpha$ value).

Figure 9 shows the q-order Hurst exponent $H(q)$ calculated by MFDFA-1. It can be seen in Figure 9 that when q is changing from -5 to 5 by increasement of $\Delta q = 1/3$, the curve of $H(q)$ for the bearing vibration acceleration signal in the normal state is different from the line of $H(q)$ for the overall faulty bearing vibration acceleration signal distribution, indicating that once the bearing fails, the internal tortuous state of the signal will change. The q-order Hurst exponent $H(q)$ of serious bearing fault signal is generally larger than that of slight bearing faults. $H(q)$ for the normal state is calculated in the range of $q \in [-5, 5]$; it is uniformly distributed. The distinction is evident when comparing with the q-order Hurst exponent $H(q)$ values of faulty signals. When $q < 0$, the $H(q)$ values for the signals of serious inner-race fault, serious outer-race fault, and serious rolling element fault are greater than the $H(q)$ values of the corresponding slight fault signals. When $q > 0$, as q increases, there appear noticeable differences of the $H(q)$ values for signals of slight inner-race fault, slight outer-race fault, and slight ball fault. Therefore, the two points at the endpoints $H(q = -5)$ and $H(q = 5)$ with the points in the middle $H(q = 0)$ can be chosen as the feature values to distinguish the degree of fault for a given value of q. In the range $q \in [-5, -4]$, the $H(q)$ values for the signals of the serious outer-race fault and the serious inner-race fault are more distinguishable from the rest of the fault signals, and the curves of the $H(q)$ values for the signals of the two ball fault signals are difficult to be distinguished from the curves of
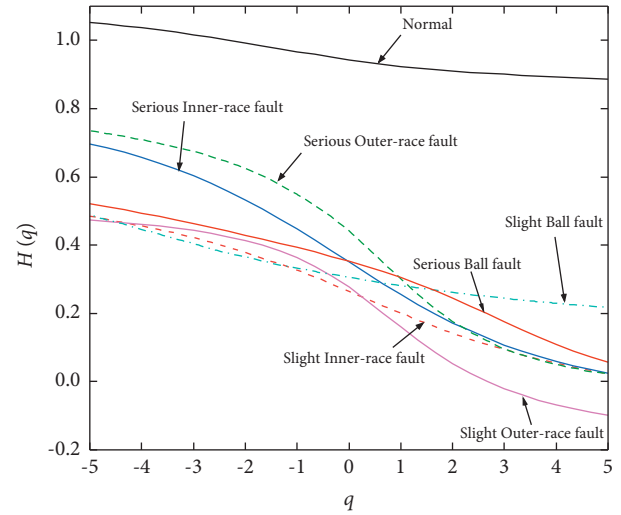
$H(q)$ values for the slight outer-race fault and the slight inner-race fault in this interval. However, with the increase of q value, the $H(q)$ values for the signal of slight ball fault do not drop as rapidly as the $H(q)$ values for the rest of the fault signals. The $H(q)$ curve of slight ball fault signal is distinguishable from that of the serious ball fault in the interval $q \in [3, 5]$. Similarly, as the value of q increases, the difference between $H(q)$ curves of the slight outer-race fault signal and serious outer-race fault signal is almost the same except in the range $q \in [-5, -2]$. Conversely, the $H(q)$ curves of signals of the two inner-race faults and the serious outer-race faults in the range $q \in [2, 5]$ are difficult to be distinguished from each other. The difference between the $H(q)$ curves of the signals of the two kinds of inner-race faults is greater in the range $q \in [-5, 0]$ than that in the interval $q \in [1, 5]$. When $q > 0$, $H(q)$ reflects the degree of fluctuation of the major trend within the signal, and when $q < 0$, $H(q)$ reflects the degree of fluctuation of the minor trend within the signal. As a result, it can be obtained that the degree of fluctuation of minor trends within the signal of serious degree of bearing fault is usually greater than that of the signal of slight degree of bearing fault when $q \in [-5, 0]$.

Figure 10 shows the singularity power spectra of seven signals based on the SPS method. In Figure 10, the characteristics of the SPS spectra of the faulty bearing signals in different states are not the same and the power spectra at specific different singularity values changed to a larger extent due to the shift in the distribution range of the singularity values. The normal bearing signal has a large singularity exponent distribution and a uniform power distribution. The distribution range of the singularity exponents of the faulty bearing signal changes, and the power distribution becomes uneven compared to the normal state. According to the occurrence of such a phenomenon, extracting the features with a large degree of variation can effectively distinguish the bearing fault and the degree of failure. The specific distribution of the 5 feature parameters $(\alpha_0, \Delta\alpha, H(q = -5), H(q = 0),$ and $H(q = 5))$ of the 70 samples (all training sets consisted of 10 sets of each state, so we get 70 sets for training) calculated by MFDFA-1 and
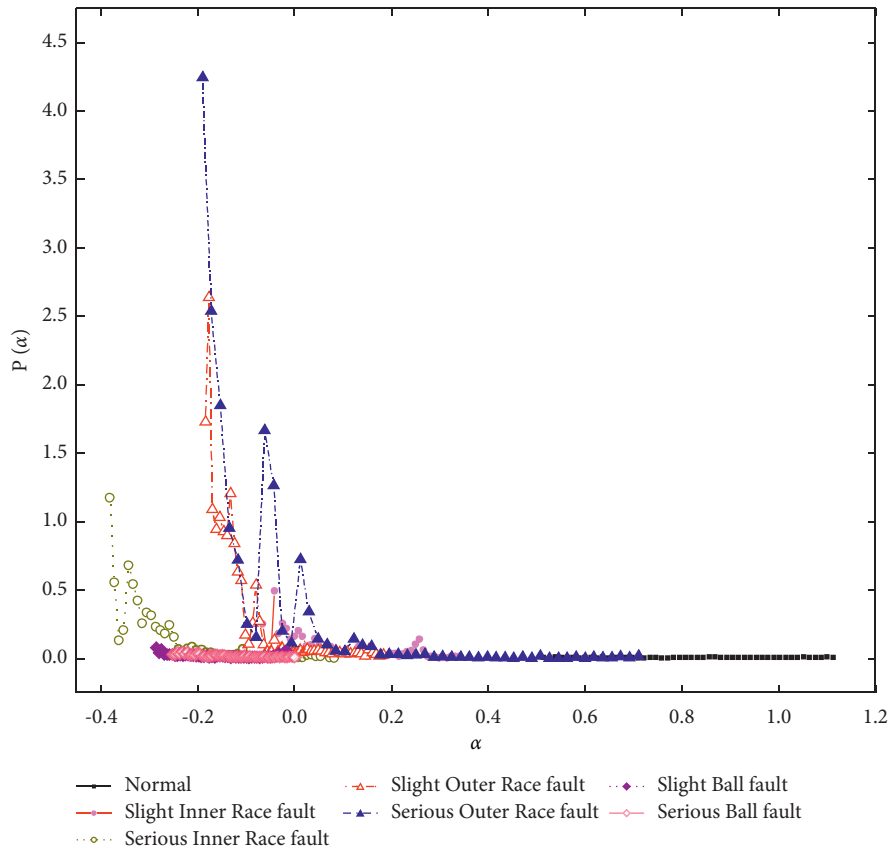
FIGURE 10: The singularity power spectra of seven signals based on the SPS method.

TABLE 2: The detailed descriptions of seven vibration signals.

Operational status	α_0	$\Delta\alpha$	$H(q = -5)$	$H(q = 0)$	$H(q = 5)$	$\sum P(\alpha)$
Normal	0.9428	0.1920	0.9709	1.0180	0.9719	0.164
	0.9015	0.0505	0.8890	0.9016	0.9220	0.1889
	0.8604	0.0810	0.8634	0.8810	0.8793	0.2001
	0.9444	0.1205	0.9494	0.9777	0.9601	0.2048
	0.879	0.2475	0.9031	1.0036	0.9064	0.187
	0.8412	0.0875	0.8521	0.8633	0.8646	0.1941
	0.8953	0.0358	0.8728	0.8839	0.9002	0.2125
	0.8845	0.1472	0.9252	0.9704	0.9296	0.1795
	0.8943	0.2320	0.9318	1.0088	0.9348	0.2152
	0.8801	0.2773	0.9592	1.0447	0.9659	0.1808
Slight inner-race fault	0.0212	0.7166	0.2469	0.4784	0.2680	3.8163
	0.017	0.7609	0.2410	0.4953	0.2626	3.4612
	0.0282	0.7446	0.2399	0.4968	0.2612	3.6263
	0.0194	0.7637	0.2446	0.4934	0.2655	3.9188
	0.0199	0.7514	0.2423	0.4926	0.2635	3.6843
	0.0338	0.7990	0.2349	0.5216	0.2558	3.9312
	0.0232	0.7452	0.2408	0.5013	0.2629	3.8348
	0.026	0.8390	0.2442	0.5325	0.2647	3.8426
	0.0206	0.7632	0.2394	0.4959	0.2606	3.7296
	0.0165	0.6942	0.2382	0.4722	0.2601	4.4186

TABLE 2: Continued.

Operational status	α_0	$\Delta\alpha$	$H(q = -5)$	$H(q = 0)$	$H(q = 5)$	$\sum P(\alpha)$
Serious inner-race fault	0.0179	1.0454	0.2957	0.6971	0.3247	6.5567
	0.0138	1.0007	0.3016	0.6499	0.3295	9.7837
	−0.0038	0.9971	0.2993	0.6581	0.3295	8.4325
	−0.0253	1.0316	0.2864	0.6547	0.3164	9.2739
	0.0035	1.0547	0.2926	0.6672	0.3211	6.15
	0.0027	0.9944	0.3019	0.6717	0.3329	7.4287
	−0.0039	1.1739	0.3056	0.7462	0.3361	5.5631
	0.0178	1.0191	0.2899	0.6604	0.3158	8.1085
	−0.0172	1.1845	0.3005	0.7466	0.3317	7.1877
	0.0032	1.1686	0.2995	0.7543	0.3297	7.1261
Slight outer-race fault	−0.113	0.8248	0.2408	0.4875	0.2780	15.47
	−0.1201	0.8391	0.2584	0.5113	0.3007	14.3396
	−0.1166	0.8249	0.2392	0.4847	0.2766	14.1815
	−0.1082	0.8311	0.2301	0.4799	0.2639	13.2106
	−0.1168	0.8655	0.2504	0.5129	0.2900	12.5522
	−0.1169	0.8559	0.2426	0.5009	0.2797	15.8954
	−0.1179	0.9478	0.2421	0.5299	0.2788	14.9106
	−0.1099	0.8490	0.2501	0.5178	0.2895	17.2239
	−0.1111	0.8175	0.2446	0.4951	0.2834	21.1568
	−0.1081	1.0547	0.2337	0.5815	0.2699	18.6271
Serious outer-race fault	−0.0035	0.9119	0.3916	0.6694	0.4321	15.9467
	−0.0135	1.1838	0.3972	0.8284	0.4442	13.4769
	−0.0468	1.0179	0.3876	0.6946	0.4304	19.988
	−0.0231	1.0009	0.3887	0.7131	0.4342	17.8346
	−0.03	1.0657	0.3965	0.7533	0.4433	17.228
	0.0041	0.9967	0.3921	0.7576	0.4387	11.4255
	−0.0169	0.9972	0.3727	0.7098	0.4144	17.3455
	−0.0311	1.0928	0.3804	0.7604	0.4261	22.7398
	−0.0226	1.0415	0.3886	0.7333	0.4342	23.2125
	−0.0111	0.9941	0.3875	0.7321	0.4340	22.9646
Slight ball fault	0.2136	0.5286	0.3091	0.4942	0.3175	0.9391
	0.2006	0.4239	0.2935	0.4254	0.3008	0.9505
	0.2255	0.3932	0.3093	0.4395	0.3166	0.8477
	0.2318	0.2892	0.2961	0.3894	0.3016	0.9875
	0.2353	0.4336	0.3075	0.4580	0.3144	0.9626
	0.245	0.2882	0.3101	0.4053	0.3158	0.9358
	0.2234	0.4132	0.3150	0.4592	0.3237	0.8414
	0.2308	0.4095	0.2942	0.4448	0.3009	0.934
	0.2447	0.4384	0.3159	0.4689	0.3227	0.8998
	0.2311	0.5342	0.3153	0.5191	0.3243	0.903
Serious ball fault	0.3011	0.5576	0.4128	0.6061	0.4229	0.6763
	0.2925	0.4627	0.3897	0.5352	0.3975	0.3966
	0.2533	0.6487	0.3998	0.5921	0.4105	0.5959
	0.2751	0.4947	0.3835	0.5475	0.3930	0.5489
	0.2931	0.4189	0.3927	0.5301	0.4013	0.6171
	0.2697	0.4043	0.3623	0.4861	0.3698	0.5054
	0.2823	0.4570	0.3861	0.5381	0.3952	0.5189
	0.2843	0.4149	0.3782	0.5047	0.3856	0.6314
	0.2821	0.3931	0.3873	0.4916	0.3944	0.8207
	0.2831	0.4511	0.3873	0.5228	0.3953	0.657

$\sum P(\alpha)$ calculated by using the SPS method are shown in Figures 10–15. The horizontal coordination denotes the number index of the sample signal. The vertical coordination denotes the feature parameter chosen for classification. The values of the six specific characteristic parameters are shown in Table 2.

In Figure 11, the normal state signal has the largest value of α_0 and the α_0 value of the signal for the occurrence of faults is smaller than the α_0 value of the normal state. Similarly, the α_0 values of the same faults at different degrees present a larger α_0 value for the signal with serious degree faults than for the signal with slight
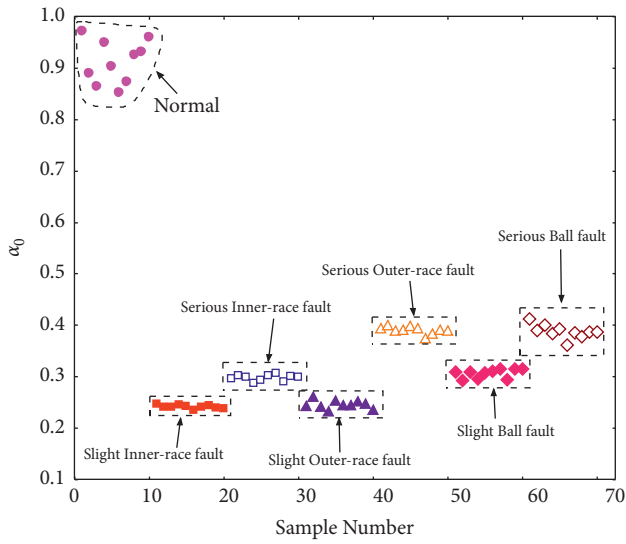
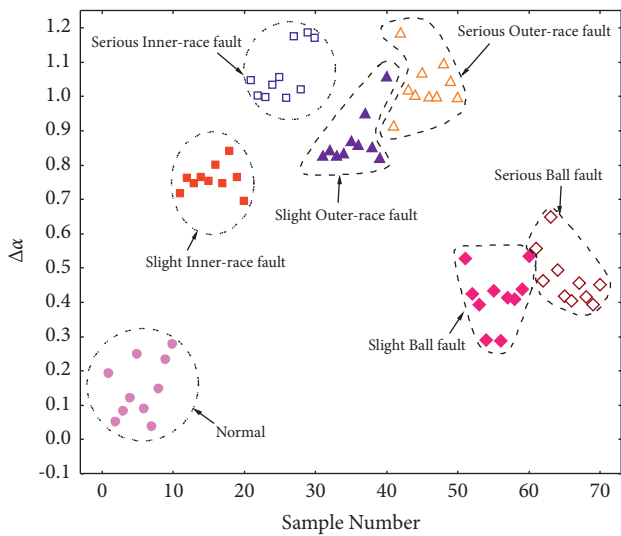FIGURE 11: The distribution range of feature α_0 calculated by MFDFA-1.

FIGURE 13: The distribution range of feature $H(q = -5)$ calculated by MFDFA-1.

FIGURE 12: The distribution range of feature $\Delta\alpha$ calculated by MFDFA-1.
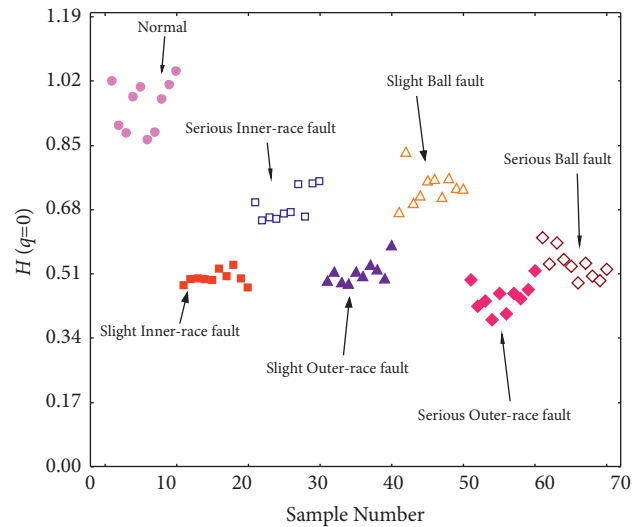
FIGURE 14: The distribution range of feature $H(q = 0)$ calculated by MFDFA-1.

degree faults. This indicates that the two parameters $\Delta\alpha$ and α_0 can be used as characteristic parameters to distinguish the normal state from fault states and also provides some possibilities to distinguish the degree of the fault as well.

In Figure 12, the distribution of $\Delta\alpha$ values for normal signals is at a low level, accompanied by an increase in $\Delta\alpha$ values in the case of faults, while the $\Delta\alpha$ values for faults of the same type but of different degrees are larger for serious faults than for slight faults.

In Figure 13, when $q = -5$, the values of the q-order Hurst exponent $H(q = -5)$ for different degrees of the same fault start to be distinguishable, especially for serious and slight faults in the inner-race as well as for serious and slight faults in the outer-race. Therefore, the q-order Hurst exponent value at
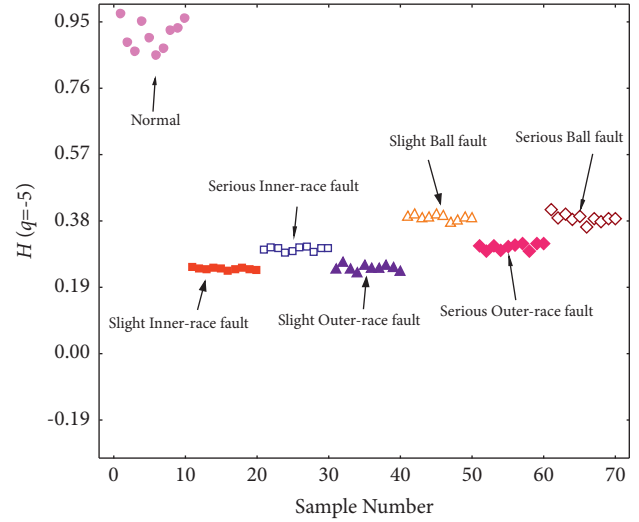
$q = -5$ is sensitive to the degree of inner- and outer-race faults and is suitable for extraction as a feature parameter.

In Figure 14, when $q = 0$, $H(q = 0)$ corresponding to serious rolling element faults can be distinguished as a whole from those corresponding to slight rolling element faults. It also shows good differentiation between serious outer-race faults and slight outer-race faults.

In Figure 15, when $q = 5$, $H(q = 5)$ for the signal of rolling element fault is relatively larger than those for the inner-race fault and outer-race fault values, but it is less sensitive to the degree of damage of the fault.

The singularity power spectra of the seven signals also exhibit distinguishability between normal and fault states. In Figure 10, the distribution of singularity exponents α for the normal state lies in the rightmost of the figure. The
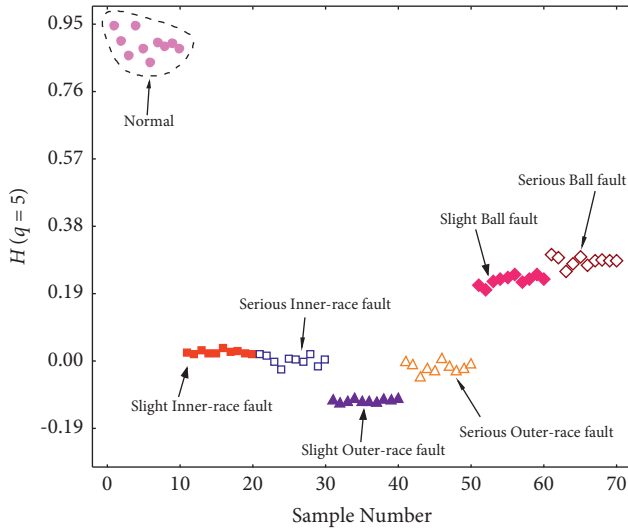
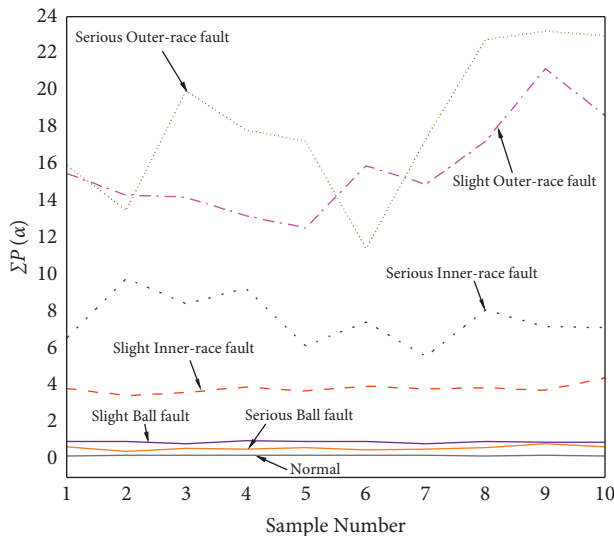Figure 15: The distribution range of feature $H(q=5)$ calculated by MFDFA-1.

Figure 16: The distribution range of feature $\sum P(\alpha)$ calculated by the SPS method.

□ Desired Output
▲ MFDFA-SPS ELM Output

Figure 17: Classification results of the ELM model based on MFDFA-SPS.

distribution of the singularity power of the signal in the normal state is flat compared to the singularity power of the signal in the faulty state. Among them, in the distribution of α, the serious inner-race fault signal lies in the leftmost of the figure, and the serious outer-race fault signal has the largest power extrema in its distribution range of α. The values of the singularity power of slight inner-race fault signal are overall smaller than those of severe degree inner-race fault signal. However, the singularity power spectra cannot be separated from each other evidently.

In Figure 16, the distribution of $\sum P(\alpha)$ for the seven states of the bearing signal is depicted. The distribution of $\sum P(\alpha)$ for serious outer-race fault signal is the widest; comparing to slight outer-race fault signal, there are crossovers existed in some samples, but the majority of
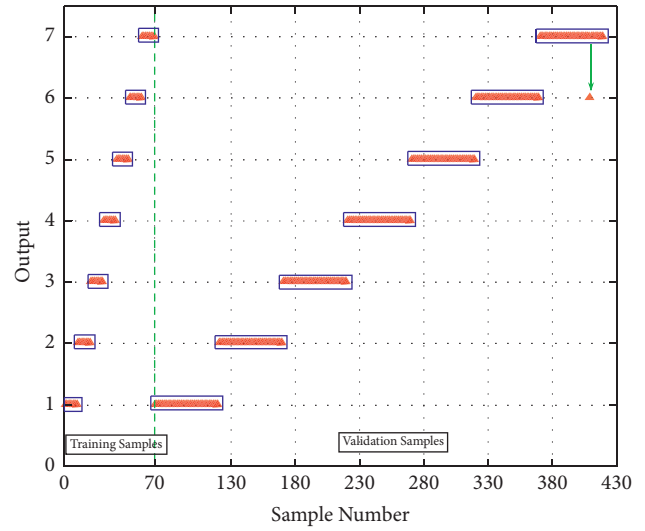
samples have greater $\sum P(\alpha)$ values than slight degrees of outer-race faults. $\sum P(\alpha)$ distinguishes the degree of two inner-race fault signals, and the distributions of both feature lines are distinguished evidently in Figure 16. Since the singularity power spectrum distribution of ball fault signal is stable, there is only a minor difference between the $\sum P(\alpha)$ feature lines of serious ball fault signal and slight ball fault signal, but $\sum P(\alpha)$ is more stable for the samples.

Some valuable patterns can be drawn from these plots; the magnitude of the spectrum vertex position α_0 usually increases as the degree of damage increases for the same fault type. The multifractal spectrum width $\Delta\alpha$ is more likely to increase for severely damaged faults than for slightly damaged faults. Except for rolling element faults, the SPS summation $\sum P(\alpha)$ feature values for severely damaged inner and outer-race faults are usually larger than those for slightly damaged inner- and outer-race faults. The above analysis proves that the six characteristics selected in this paper can effectively quantify the types of bearing faults and the degrees of damage.

According to the representation law of these six features, the six parameters are composed into a vector to represent the different bearing state characteristics.

For classification of types using ELM, the number of hidden neurons is 50 and the transfer function is sigmoidal function. The training set consisting of 70 samples is fed into the ELM classifier, and the remaining samples after segmenting the data are used as the test set. The ELM classification results are shown in Figure 17. Similarly, the training set is trained using SVM and LSSVM tools, respectively, and the same is verified for the test set. The classification results obtained are shown in Figures 18 and 19. In the multi-classification problem of bearing faults using SVM, Support Vector Machine for Regression (SVR) is chosen. The kernel function is chosen as radial basis function with a gamma
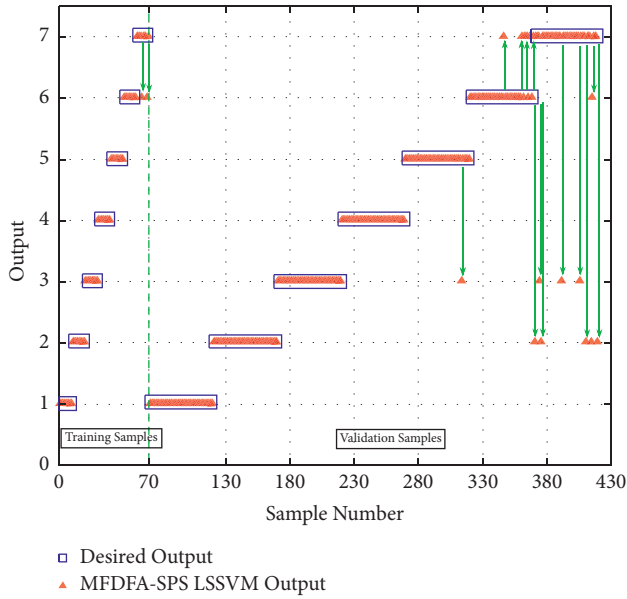
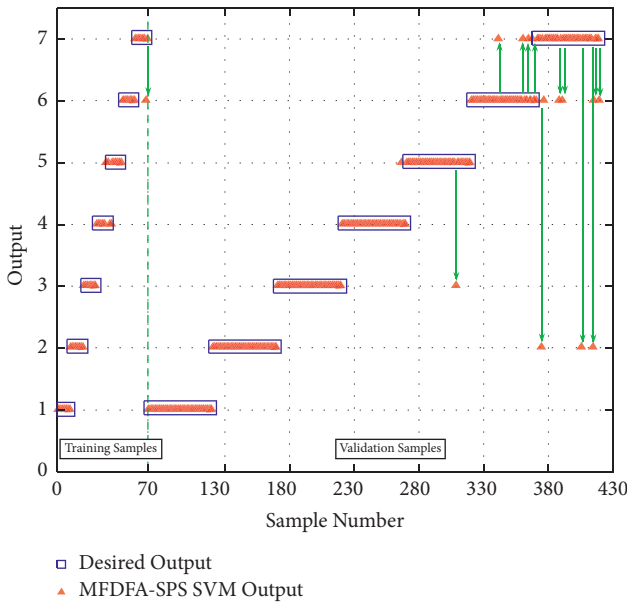Figure 18: Classification results of the LSSVM model based on MFDFA-SPS.

Figure 20: Classification results of the ELM model based on MFDFA.

Figure 19: Classification results of the SVM model based on MFDFA-SPS.
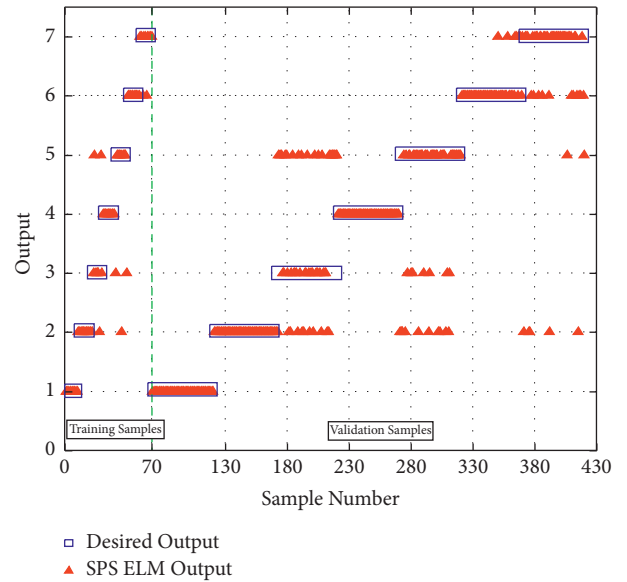
Figure 21: Classification results of the ELM model based on SPS.

Table 3: Average runtime and recognition accuracy of five methods.

Algorithm	Average runtime (s)	Average recognition accuracy (%)
MFDFA + ELM	54.41	92.46
SPS + ELM	2.05	80.83
MFDFA-SPS + ELM	54.56	99.25
MFDFA-SPS + LSSVM	55.52	95
MFDFA-SPS + SVM	54.22	95.71

parameter coefficient of 0.05. For classification of fault signals using LSSVM, the optimization function is chosen as simplex, and the training and test sets are classified using a cross-validation method.

As can be seen in Figures 20 and 21, we have 7 kinds of signals in different states; the validation acceleration data of each state are divided into 50 sets, so we can get 350 sets. All training sets consisted of 10 sets of each state, so we get 70 sets for training, and the number of total test sets is 350. The average runtime and correct recognition rates of five methods are shown in Table 3. The diagnostic results of the
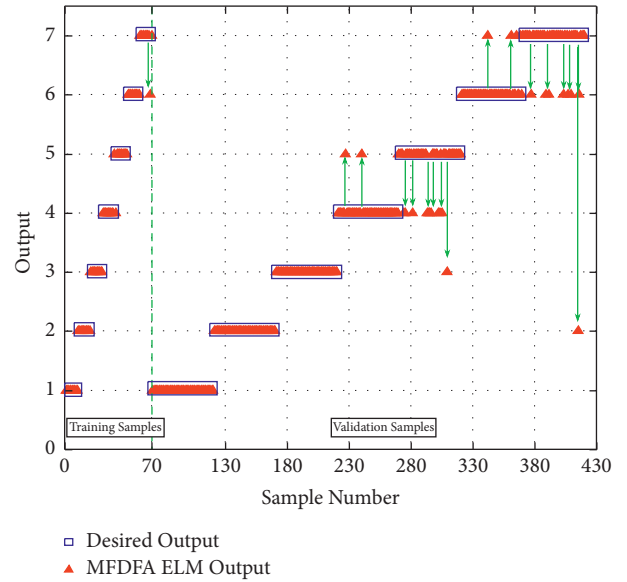
five classification tools illustrate that this feature extraction method can distinguish different kinds of bearing fault signals with different faults. Among the ELM classifier

results, there are no errors in the test set except for only one data belonging to the serious rolling element fault in the test set is classified into the slight rolling element fault with a correct rate of 99.25%. In the results obtained by the MFDFA-SPS-based detection method with SVM classification, the highest probability of errors was found for ball faults, with an overall correct rate of 95%. In the LSSVM classification results, the correct rate also reached 95.71% due to the excessive number of parameters that needed to be preset and did not have optimization.

Therefore, based on the overall classification correctness, it can be obtained that the MFDFA-SPS-based feature extraction method can be applied to the fault diagnosis of bearings, and the classification method can be further optimized to achieve better classification results.

6. Conclusions

Based on the above study, the following conclusions can be drawn:

(1) By applying the bearing faults from the Case Western Reserve database, the bearing fault diagnosis method combining MFDFA with SPS and ELM can be applied to diagnose different faults as well as faults with different damage levels

(2) The MFDFA-SPS fault feature extraction method based on ELM does not require preprocessing of fault data and is suitable for real-time monitoring of the operation status of bearing faults

If only SPS is used to extract the specific feature parameters of the faulty bearing because the distribution range of the singularity values of different degrees of the faulty signal is different (except for some serious faulty signals), it will cause the stacking of different signal spectrum lines in different intervals of distribution, and the intuitive spectrum line discrimination is not strong only from the graph, so we need to combine other feature extraction methods and choose a more effective classifier for classification to achieve a better classification effect on the rolling bearing signal.

The proposed method has 3 advantages. First, the proposed method has no preprocessing procedure for the sampled data, which substantially reduces the complexity of the overall diagnostic process. Second, the feature extraction time using the MFDFA-SPS algorithm is short, which improves the efficiency of online fault diagnosis. The various bearing signal data used in this paper have only 2048 points, and the need for fault diagnosis can be achieved in a short time. Finally, the effect of classification can reach more than 99%, which ensures the reliability of the diagnosis method. Therefore, the proposed method is suitable for application to practical engineering problems.

With the approach proposed in the above section, we can still achieve good diagnostic results based on the Case Western Reserve bearing database using a smaller number of training set. The future direction of research is to test the sensitivity of this method to the feature extraction and fault diagnosis effect of different bearing vibration signals, as well

as to realize the composite fault diagnosis of different faults superimposed.

Data Availability

The acceleration data of the bearings used to support the findings of this study have been deposited on the Case Western Reserve University Bearing Data Center website (https://engineering.case.edu/bearingdatacenter/).

Conflicts of Interest

The authors declare that they have no conflicts of interest.

Acknowledgments

References

[1] J. Gegner, *Tribological Aspects of Rolling Bearing Failures*, Tribology-Lubricants and Lubrication, Taiwan, 2011.

[2] R. B. Randall and J. Antoni, "Rolling element bearing diagnostics-A tutorial," *Mechanical Systems and Signal Processing*, vol. 25, no. 2, pp. 485–520, 2011.

[3] B. B. Mandelbrot, "How long is the coast of britain? Statistical self-similarity and fractional dimension," *Science*, vol. 156, no. 3775, pp. 636–638, 1967.

[4] B. B. Mandelbrot, *Multifractals and 1/f Noise: Wild Self-Affinity in Physics (1963–1976)*, Springer, New York, NY, USA, 2013.

[5] B. B. Mandelbrot and J. W. V. Van Ness, "Fractional brownian motions, fractional noises and applications," *SIAM Review*, vol. 10, no. 4, pp. 422–437, 1968.

[6] T. Harris and M. Kotzalas, *Advanced Concepts of Bearing Technology*, 2006.

[7] J. Antonia and R. B. Randall, "The spectral kurtosis: application to the vibratory surveillance and diagnostics of rotating machines," *Mechanical Systems and Signal Processing*, vol. 20, pp. 308–311, 2004.

[8] Q. Ni, J. C. Ji, and K. Feng, "Data-driven prognostic scheme for bearings based on a novel health indicator and gated recurrent unit network," *IEEE Transactions on Industrial Informatics*, p. 1, 2022.

[9] K. Feng and W. A. Smith, "Use of cyclostationary properties of vibration signals to identify gear wear mechanisms and track wear evolution," *Mechanical Systems and Signal Processing*, vol. 150, pp. 1–24, Article ID 107258, 2020.

[10] J. Shao, X. Pang, Z. Yang, and J. Li, "Research on Intelligent Recognition of axis Orbit Based on Hu Moment Invariants and Fractal Box Dimension," in *Proceedings of the 2017 14th International Conference on Ubiquitous Robots and Ambient IntelligenceURAI*, June 2017.

[11] H. Liu, X. Wang, and C. Lu, "Rolling bearing fault diagnosis based on LCD-TEO and multifractal detrended fluctuation analysis," *Mechanical Systems and Signal Processing*, vol. 60-61, pp. 273–288, 2015.

[12] J. Lin and Q. Chen, "Fault diagnosis of rolling bearings based on multifractal detrended fluctuation analysis and

Mahalanobis distance criterion," *Mechanical Systems and Signal Processing*, vol. 38, no. 2, pp. 515–533, 2013.

[13] Q. Chen, L. Hongru, and X. Baohua, "Fault prediction for bearings based on morphological fractal dimension and improved ELM," *Bearing*, vol. 4, pp. 45–49, 2014.

[14] Q. Xiong, W. Zhang, and T. Lu, "A fault diagnosis method for rolling bearings based on feature fusion of multifractal detrended fluctuation analysis and alpha stable distribution," *Shock and Vibration*, vol. 2016, Article ID 1232893, 12 pages, 2016.

[15] Y. Zhao and K. Yu, "Joint domain alignment and class Alignment method for cross-domain fault diagnosis of rotating machinery," *IEEE Transactions on Instrumentation and Measurement*, vol. 70, Article ID 3526212, 2021.

[16] E. Ihlen, "Introduction to multifractal detrended fluctuation analysis in Matlab," *Frontiers in Physiology*, vol. 3, p. 141, 2012.

[17] G. Xiong, W. Yu, and S. Zhang, "Singularity power spectrum distribution," *Physica A: Statistical Mechanics and Its Applications*, vol. 431, pp. 63–73, 2015.

[18] G. Huang, Q. Zhu, and C. Siew, "Extreme learning machine: theory and applications," *Neurocomputing*, vol. 70, no. 1-3, pp. 489–501, 2006.

[19] I. J. Good and B. B. Mandelbrot, "Fractals: form, chance, and dimension," *Journal of the American Statistical Association*, vol. 32, pp. 73–438, 1978.

[20] H. Ocak and K. A. Loparo, "Estimation of the running speed and bearing defect frequencies of an induction motor from vibration data," *Mechanical Systems and Signal Processing*, vol. 18, no. 3, pp. 515–533, 2004.

[21] Cwru Dataset, "Case western Reserve university bearing data center," 2022, https://csegroups.case.edu/bearingdatacenter/home.